Acta Cryst. (1981). B37, 793–803

New Series of Long-Period α-PbO_2-Related Intergrowth Structures in the System $(Cr,Fe)_2O_3$–$(Ti,Zr)O_2$*

BY IAN E. GREY

CSIRO Division of Mineral Chemistry, PO Box 124, Port Melbourne, Victoria, Australia 3207

(*Received* 7 *August* 1980; *accepted* 27 *October* 1980)

Abstract

New series of compounds (*I* phases) have been prepared in the Cr_2O_3–Fe_2O_3–TiO_2–ZrO_2 system by reacting mixtures corresponding to the compositions $(Cr_{1-x}Fe_x)_2(Ti_{1-y}Zr_y)_3O_9$, $x = 0{\cdot}0$–$0{\cdot}5$, $y = 0{\cdot}15$–$0{\cdot}25$, in nitrogen at temperatures in the range 1853–1923 K. The diffraction patterns could be indexed completely using the indexing scheme $(h_\alpha \pm n.\xi, k_\alpha \pm m.\delta, l_\alpha)$, n and m integers, where $(h_\alpha,k_\alpha,l_\alpha)$ refer to an α-PbO_2-type subcell and ξ, δ are two vectors used to measure the superlattice spot positions along $[100]_\alpha$ and $[010]_\alpha$. For different preparations, ξ and δ had values in the ranges $0{\cdot}195$–$0{\cdot}227$ and $0{\cdot}179$–$0{\cdot}223$ respectively, and were linearly dependent for fixed x in the above formula. Idealized models for the structures of the *I* phases in the approximation of simple fractional values of ξ and δ $(\frac{1}{4},\frac{1}{5},\frac{1}{6},\frac{1}{7})$ have been established. These models show that the main structural features of the *I* phases may be derived by an ordered occupation of approximately $\frac{5}{9}$ of the octahedral sites in a hexagonal close-packed oxygen lattice, to produce blocks comprising strings of α-PbO_2-type and corundum-type structural elements intergrown parallel to $[110]_\alpha$ and $[1\bar{1}0]_\alpha$. These blocks are parallel to $(100)_\alpha$ and infinitely extended along $[010]_\alpha$ and $[001]_\alpha$. The metal-atom arrangements in the blocks are mirrored across $(100)_\alpha$ planes containing α-PbO_2-like edge-shared chains of octahedra, parallel to $[001]_\alpha$. These chains in the metal mirror planes corner link to similar chains in the adjacent blocks to produce columns of α-PbO_2 type, infinitely extended along $[001]_\alpha$. The observed values of ξ and δ could be explained by ordered long-periodicity variations in both the metal-mirror-plane separations and in the widths of the α-PbO_2-type and corundum-type elements in the intergrowth blocks. Unit-cell compositions have been derived for the structural models, for the observed ranges of values of ξ and δ and some structure–composition relationships are discussed. In particular, the relationship between the vectors ξ and δ is explained in terms of the requirement of ordering of Zr and Ti in the α-PbO_2 columns of the structures.

1. Introduction

In the Cr_2O_3–TiO_2 system, a compound with formula $Cr_2Ti_2O_7$ was first identified by Hamelin (1957). The presence of this so called *E* phase was confirmed in the studies by Lee (1970) and Flörke & Lee (1970), who found that the phase had a range of homogeneity which increased with increasing temperature. Grey & Reid (1972) studied the formation of the *E* phase in the system Fe_2O_3–Cr_2O_3–TiO_2. For the composition with equi-atomic amounts of Fe and Cr, *i.e.* $FeCrTi_2O_7$, they were able to grow crystals large enough for a single-crystal X-ray diffraction study. The structure of $CrFeTi_2O_7$ (Grey & Mumme, 1972) could be described as an ordered intergrowth of TiO_2 with the α-PbO_2 structure, and $CrFeTiO_5$, with the V_3O_5 structure, parallel to $(110)_{\alpha\text{-}PbO_2}$. The observed homogeneity range for the *E* phase could then be described in terms of a continuous series of ordered intergrowths of different-width slabs of α-PbO_2 and V_3O_5 structural types, having the general formula $pM_3O_5.qM_2O_4$ or, more specifically, $(Cr,Fe)_{2p}Ti_{p+2q}O_{5p+4q}$ where p and q are integers, *e.g.* for $Cr_2Ti_2O_7$, $p = 2$, $q = 1$. In the system Cr_2O_3–Fe_2O_3–TiO_2, members of the series with $q \precsim p$ only could be prepared. It was found that addition of ZrO_2 allowed intergrowths with higher q/p ratios to be stabilized, *i.e.* with higher relative amounts of α-PbO_2 component. Zirconia-stabilized members of the intergrowth series were characterized for q/p ratios from 4/3 to 5/2 (Grey, Reid & Allpress, 1973).

In the studies reported in this paper the zirconia-substitution experiments have been extended to compositions with lower q/p ratios. It was found that for compositions with q/p close to one, the replacement of Ti by Zr resulted in the formation of new phases with X-ray powder diffraction patterns considerably different from those for the α-PbO_2–V_3O_5 intergrowths. It

* Work done in part while the author was at Laboratoire de Cristallographie, CNRS, 166 X, 38042 Grenoble CEDEX, France.

0567-7408/81/040793-11$01.00

was observed that small changes in the metal-atom ratios and in the preparation temperature produced significant changes in the powder patterns, characteristic of another ordered intergrowth series. For compositions with about 20 at.% replacement of Ti by Zr and at temperatures close to 1873 K, the new phases were prepared in a pure state. Electron and X-ray single-crystal diffraction patterns showed complex planar arrays of superlattice reflections with spacings which were not simple fractions of the subcell repeat distances. The separation between these planes corresponded to a 5·0 Å period, which is an axis common to the α-PbO_2–V_3O_5 intergrowth structures. It was found that the diffraction patterns could be indexed completely in relation to an α-PbO_2 subcell, using two vectors, δ and ξ, to define the superlattice spot positions. The structure of one of the *I* phases* has been determined in the approximation of $\delta = \xi = \frac{1}{5}$, and modifications to this idealized 'basis-structure' to explain the observed complex values of ξ and δ have been considered. The structural principles underlying the new series of α-PbO_2-related superstructures are presented in this paper.

2. Experimental

The chemicals used in this work were Fisher Certified TiO_2 (anatase form), ZrO_2 and Fe_2O_3, together with Cr_2O_3 prepared in a finely divided, reactive form by decomposing analytical grade ammonium dichromate, heated finally at 1173 K for 30 min. Finely ground, pelletized mixtures of the component oxides were supported in recrystallized alumina boats and heated in a nitrogen atmosphere for periods of up to 18 h, then cooled quickly to room temperature. The heat treatment was performed in a Mo wound furnace fitted with a recrystallized alumina work-tube. Temperatures were controlled within ± 5 K during the heat treatment.

The reaction products were identified from their powder X-ray diffraction patterns, obtained using a Philips diffractometer fitted with a graphite monochromator. For the single-phase products, potassium chloride was added as an internal standard and diffractograms were obtained at a scan rate of 0·25° min^{-1} for lattice parameter determination. Where suitable single crystals formed in the reaction products, they were examined by single-crystal X-ray diffraction, using the precession method. Electron diffraction patterns were obtained for two of the single-phase preparations by Dr M. A. Alario-Franco, using a Siemen's Elmiskop-102 electron microscope.

Selected single-phase reaction products were analysed for Fe, Cr, Ti and Zr, using a JXA 50A electron microprobe, with haematite, $MgCr_2O_4$, rutile and zirconia as standards. The analyses were necessary because significant losses of Cr as the volatile species $CrO_3(g)$ occur at the high temperatures used in this study, *cf.* Somiya, Hirano & Kamiya (1978) who measured a weight loss of 11·1% on heating a Cr_2O_3/TiO_2 mixture containing 29 mol% Cr_2O_3 to 1923 K in air for 24 h. This corresponds to a loss of 16·6% of the original chromium oxide as $CrO_3(g)$.

Sectioned pellets of the reaction products were also examined in a JSM-U3 scanning electron microscope fitted with a high-sensitivity back-scattered electron detector (Robinson & Nickel, 1979) and X-ray analyser. Particular care was taken to check for Cr composition gradients due to volatilization.

3. Results

3.1. *Stability region for the I phase*

The results from equilibration runs carried out in the present study, summarized in Table 1, indicate the effect of temperature and composition variables on the domain of stability of the *I* phases. Although considerably more experimental work would be required to define precisely the phase equilibria, the general conclusion from the exploratory work summarized in Table 1 is that at temperatures near 1873 K in nitrogen, the *I* phases occupy a narrow compositional region of stability, centred on a composition with 60 mol% TiO_2, 20 mol% Cr_2O_3, 15 mol% ZrO_2 and 5 mol% Fe_2O_3, *i.e.* $(Cr_{0.8}Fe_{0.2})_2(Ti_{0.8}Zr_{0.2})_3O_9$. Some specific observations are listed below:

(*a*) The region of stability for the *I* phases was found to be particularly sensitive to the Zr concentration. The results for equilibration runs *C* and *F*, Table 1, show that a variation of the [Zr]/([Zr] + [Ti]) ratio by 0·05 from the mean value of 0·20 resulted in formation of a second phase. For decreased Zr contents the second phase was the *E* phase, *i.e.* a member of the series $(Cr,Fe)_{2p}(Ti,Zr)_{p+2q}O_{5p+4q}$, consistent with our previous studies (Grey *et al.*, 1973). For higher Zr contents, *i.e.* [Zr]/([Zr] + [Ti]) > 0·20, the monoclinic form of ZrO_2, baddeleyite, precipitated. The *I* phase stability was not as sensitively dependent on the Fe to Cr ratio. Single-phase material could be obtained at [Fe]/([Fe] + [Cr]) ratios from 0·00 up to 0·30 by varying the reaction temperature and time. Higher Fe contents resulted in the formation of both a fluorite-related phase and a phase with a powder pattern similar to that of nolanite (Robinson, Evans, Schaller & Fahey, 1957) (presumably with Ti in place of V).

(*b*) The range of oxygen to metal ratios for formation of the *I* phases was limited to values close to 1·80, *i.e.*

* The new series of α-PbO_2-related incommensurate superstructures described in this paper are designated in abbreviated form as *I* phases. We have retained Hamelin's use of *E* phase to indicate the α-PbO_2–V_3O_5 intergrowth phases previously described (Grey *et al.*, 1973).

Table 1. *Phase relations in the system* $(Cr,Fe)_2O_3$–$(Ti,Zr)O_2$

Run	Composition of reaction mixture: [Fe]/([Fe] + [Cr])	[Zr]/([Zr] + [Ti])	$[M^{3+}]/\sum[M]$	O/M	Temperature (K)	Reaction time (h)	Reaction products by XRD
A-1	0·20	0·20	0·40	1·80	1853	4	*I*[a]
-2	0·30	0·20	0·40	1·80	1853	4	*I* + *F* (trace)
-3	0·50	0·20	0·40	1·80	1853	4	*I* + *F* + *N*
B-1	0·00	0·20	0·40	1·80	1853	18	*E* + Cr_2O_3 + *I* (trace)
-2	0·20	0·10	0·40	1·80	1853	18	*E*
-3	0·20	0·20	0·40	1·80	1853	18	*I*
-4	0·30	0·20	0·40	1·80	1853	18	*I*
C-1	0·00	0·15	0·40	1·80	1893	2	*I* + *E*
-2	0·00	0·20	0·40	1·80	1893	2	*I*
-3	0·00	0·25	0·40	1·80	1893	2	*I* + ZrO_2
-4	0·20	0·20	0·40	1·80	1893	2	*I*
D-1	0·00	0·10	0·40	1·80	1863	3	*E*
-2	0·00	0·20	0·40	1·80	1863	3	*I* + *E* (trace) + ZrO_2 (trace)
-3	0·00	0·15	0·50	1·75	1863	3	*E* + *I* + Cr_2O_3
E-1	0·00	0·20	0·33	1·84	1893	4	*E*
-2	0·00	0·20	0·40	1·80	1893	4	*I* + *E* (minor)
-3	0·00	0·15	0·50	1·75	1893	4	*E* + Cr_2O_3 + *I* (trace)
-4	0·20	0·20	0·40	1·80	1893	4	*I*
F-1	0·00	0·15	0·40	1·80	1903	5	*E* + *I* (minor)
-2	0·00	0·20	0·40	1·80	1903	5	*I*
-3	0·00	0·25	0·40	1·80	1903	5	*I* + ZrO_2
G-1	0·00	0·20	0·40	1·80	1923	3	*I*
H-1[b]	0·00	0·20	0·40	1·80	1893	2	*I* + *E* + ZrO_2
-2	0·20	0·20	0·40	1·80	1893	2	*I* + *E*
-3	0·20	0·15	0·50	1·75	1893	2	*I* + *E* + ZrO_2

(*a*) *I* = incommensurate superstructure, $E = (Cr,Fe)_{2p}(Ti,Zr)_{p+2q}O_{5p+4q}$ (Grey *et al.*, 1973), *N* = nolanite-type structure (Robinson *et al.*, 1957), *F* = fluorite-type structure. (*b*) Reaction in air.

$[M^{3+}]/\sum[M] = 0{\cdot}40$, as evidenced by the extra phases produced when the M^{3+}/M^{4+} ratio was changed (Table 1). The formation of *E* phases for O/*M* ratios higher than 1·80 is consistent with our earlier phase and structural studies (Grey *et al.*, 1973), where zirconia-stabilized *E* phases were characterized for O/*M* ratios in the range 1·823 to 1·875. For O/*M* ratios lower than about 1·80, Cr_2O_3 appeared in the reaction product.

(*c*) The *I* phases were stable in nitrogen from about 1853 K up to the highest temperature used in this study, 1923 K. At temperatures lower than 1853 K, the *I* phases were unstable relative to mixtures of *E* phases plus the monoclinic form of ZrO_2. A series of reactions carried out in air at 1923 K (*H*-1 to *H*-3, Table 1), also gave *E* phases plus zirconia as the major products, indicating that higher temperatures are needed to form pure *I* phases in air compared with nitrogen.

3.2. *Stoichiometry and homogeneity of samples*

Reaction products which appeared to be single-phase from XRD studies were further examined in a scanning electron microscope fitted with an energy dispersive analyser for X-rays. The samples were found to be homogeneous and the only detectable impurity was occasional small particles (~10 μm) of ZrO_2 which appeared as bright specks in the back-scattered electron images.

Four samples were selected for detailed microprobe analyses; *F*-2 and *G*-1 from starting composition $Cr_2Ti_{2.4}Zr_{0.6}O_9$ and *A*-1 and *B*-3 from $Cr_{1.6}Fe_{0.4}Ti_{2.4}Zr_{0.6}O_9$ (see Table 1). Analyses were performed on both the rims and the centres of the reaction pellets to check for zoning. The results are summarized in Table 2. The loss of Cr due to volatilization is evident, with Cr analyses for all samples being significantly below theoretical. The effect of increased reaction time at fixed temperature is seen by comparing *A*-1 with *B*-3; the average wt% Cr (average of both rim and core values) decreased from 29·01 to 28·49% after heating for 4 h at 1853 K and to 27·63% after a further 12 h at the same temperature. The losses are much lower than those observed by Somiya *et al.* (1978), due to the combined effect of lower Cr contents in our samples and lower O fugacities above our reaction mixtures.

A small but consistent zoning of Cr is observed in all the samples, with maximum Cr loss at the rims of the

Table 2. *Electron microprobe analyses* (*wt* %)

Compositions, normalized to 3(Ti + Zr), are:

F-2	$Cr_{1\cdot95}Ti_{2\cdot39}Zr_{0\cdot61}O_{8\cdot92}$	$O/M = 1\cdot80$
G-1	$Cr_{1\cdot95}Ti_{2\cdot42}Zr_{0\cdot58}O_{8\cdot92}$	$O/M = 1\cdot80$
A-1	$Cr_{1\cdot57}Fe_{0\cdot39}Ti_{2\cdot38}Zr_{0\cdot62}O_{8\cdot94}$	$O/M = 1\cdot80$
B-3	$Cr_{1\cdot52}Fe_{0\cdot40}Ti_{2\cdot40}Zr_{0\cdot60}O_{8\cdot88}$	$O/M = 1\cdot80$

Sample	Cr_2O_3	Fe_2O_3	TiO_2	ZrO_2	Total
F-2 core (3)[a]	35·70		45·16	17·97	98·83
rim (3)	35·22		45·95	18·17	99·34
G-1 core (2)	35·35		45·95	17·15	98·45
rim (1)	35·03		46·08	16·52	97·63
$Cr_2Ti_{2\cdot4}Zr_{0\cdot6}O_9$	36·39		45·91	17·70	
A-1 core (2)	28·73	7·49	45·29	17·55	99·06
rim (2)	28·25	7·29	45·72	18·88	100·14
B-3 core (3)	27·80	7·72	45·62	17·88	99·02
rim (3)	27·46	7·51	45·79	17·77	98·53
$Cr_{1\cdot6}Fe_{0\cdot4}Ti_{2\cdot4}Zr_{0\cdot6}O_9$	29·01	7·61	45·74	17·64	

(*a*) Analyses given are averages of the number of individual analyses shown in parentheses.

pellets. Both Ti and Zr were generally enriched at the rim, relative to the centre of the pellets. In *G*-1, which was an exception in having lower Zr contents than theoretical, small exsolved grains of ZrO_2 were observed in the SEM.

Compositions which have been normalized to maintain the same number of atoms of Ti plus Zr as in the starting mixtures (*i.e.* three) are given in Table 2. The actual O contents are expected to be lower than indicated due to partial reduction of Fe to Fe^{2+}, as well as possible slight reduction of Ti and Cr to Ti^{3+} and Cr^{2+} respectively. Because of the extremely refractory nature of the phases, we were unable to analyse for reduced species by using wet-chemical procedures.

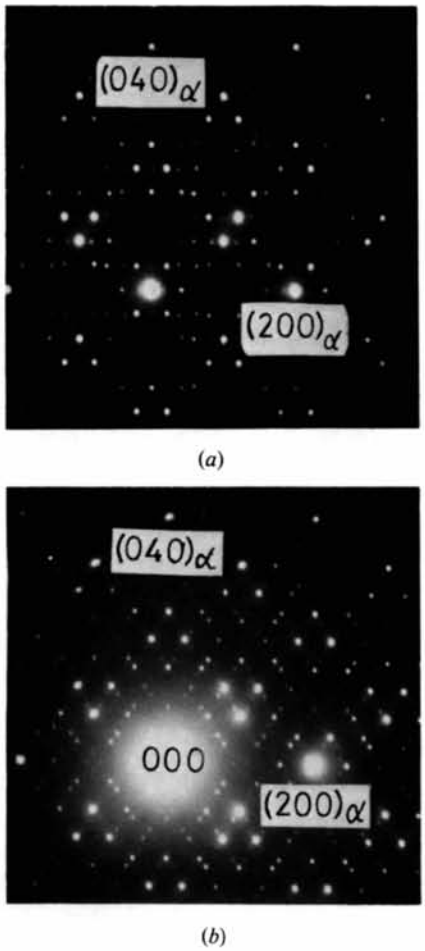

Fig. 1. $[001]_\alpha$ zone-axis diffraction patterns for *I* phases. (*a*) Sample *B*-3, see Table 1, (*b*) sample *C*-4, Table 1.

3.3. *Diffraction results*

Typical electron diffraction reciprocal-lattice sections perpendicular to the 5 Å zone axis are shown in Fig. 1 for *I* phases resulting from runs *B*-3 and *C*-4 in Table 1. At first glance the two patterns appear to have little in common. Much of the complexity is due to the interpenetration of clusters of superlattice spots centred around each subcell node; for electron diffraction, the higher-order superlattice reflections have artificially high intensities and the interpenetration patterns mask the underlying relationships between the basic patterns.

Fig. 2(*a*) is a schematic representation of the 5 Å zone-axis pattern for an *I* phase (from run *E*-4), traced directly from a precession photograph; the observed intensities have been reduced to F^2 and are approximated by the areas of the diffraction spots. Some time was spent in attempts to establish a subcell passing through the strongest reflections. Eventually it was realized that the geometrical centres of gravity of the various clusters of strongest reflections lay on the nodes of a simple orthogonal cell. The cell outline is marked on Fig. 2(*a*); the corresponding real-space cell dimensions are 4·70 × 5·60 × 5·0 Å (zone axis). These dimensions correspond closely to those of α-PbO_2-type structures, such as the high-pressure form of TiO_2 (McQueen, Jamieson & Marsh, 1967) and $ZrTiO_4$ (Coughanour, Roth & De Prosse, 1954). Using the α-PbO_2 subcell indices, $(h_\alpha,k_\alpha,l_\alpha)$ together with two r.l. vectors ξ and δ to define the superlattice spot positions, all reflections in the single-crystal diffraction patterns could be indexed as $(h_\alpha \pm n.\xi, k_\alpha \pm m.\delta, l_\alpha)$ where m and n are integers. Using this indexing scheme we were able to index completely the powder patterns for the *I* phases and obtain precise values for $a_\alpha,b_\alpha,c_\alpha$ from least-squares refinement of the powder data. The values of ξ and δ were then optimized by hand calculation. Their associated error is estimated to be $\pm 0\cdot001$. An example of an indexed powder pattern is given in Table 3. In Table 4 are listed the refined values for the five parameters, obtained for the single-phase products listed in Table 1. It is seen that for a fixed starting composition, the parameters are a sensitive function of the reaction conditions, *i.e.* temperature and

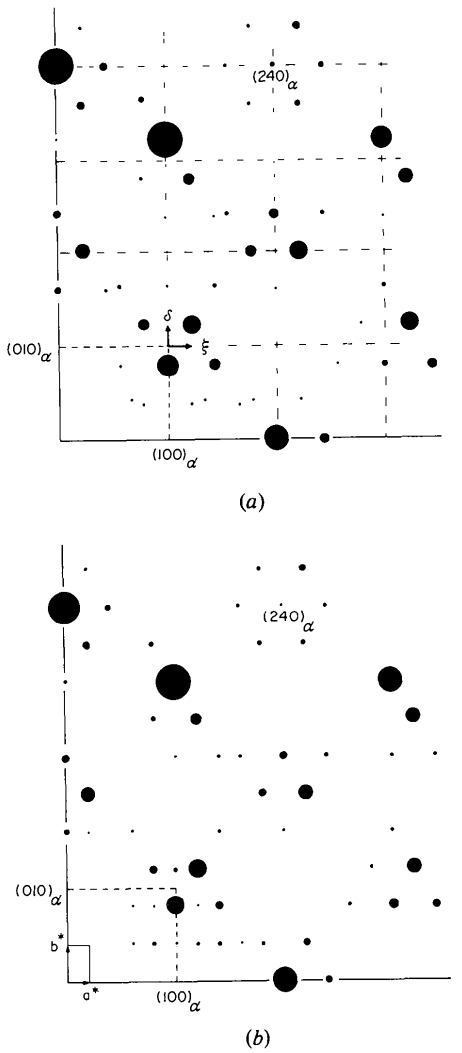

Fig. 2. (*a*) Observed and (*b*) calculated *hk*0 diffraction patterns. The observed intensities, measured off precession photographs for sample *E*-4 (Table 1), were reduced to F^2's; their magnitudes are represented by the filled circles. The calculated distribution of F^2's in (*b*) is for a model with $\xi = \delta = \frac{1}{3}$. The α-$PbO_2$ subcell is shown by the dashed lines.

Table 3. *X-ray powder diffraction data for an I phase (from run E-4 in Table 1)*

h	*k*	*l*	d_c (Å)	d_o (Å)	I_{rel}
1	$1-\delta$	0	3·914	3·916	42
$1-\xi$	$1+\delta$	0	3·671	3·672	8
$1-\xi$	$1-\delta$	1	3·377	3·375	16
$1+\xi$	$1+\delta$	0	2·975	2·973	26
$1+\xi$	$1-\delta$	1	2·812	2·810	55
1	$1+\delta$	1	2·761	2·760	100
0	0	2	2·509	2·508	26
0	2	1	2·443	2·442	64
2	0	0	2·355	2·355	26
1	2	1	2·168	2·168	70
1	$1-\delta$	2	2·112	2·113	10
$1+\xi$	$1+\delta$	2	1·918	1·918	23
$2-\xi$	2	0	1·919		
ξ	2	2	1·861	1·860	11
2	0	2	1·717	1·717	38
2	2	1	1·695	1·695	100
$2+\xi$	2	0	1·692		
1	$3+\delta$	0	1·6359	1·6363	24
$1+\xi$	$1-\delta$	3	1·5006	1·5009	5
1	$1+\delta$	3	1·4927	1·4932	14
0	2	3	1·4359	1·4356	32
3	$1+\delta$	1	1·4260	1·4260	12
0	4	0	1·3981	1·3985	9
$3+\xi$	$1-\delta$	1	1·3790	1·3787	7
1	$3+\delta$	2	1·3706	1·3708	36
ξ	4	1	1·3442	1·3443	9

Table 4. *Subcell parameters and vectors ξ, δ for I phases*

Sample	a_α (Å)	b_α (Å)	c_α (Å)	ξ	δ
C-2	4·678 (1)	5·596 (1)	5·008 (1)	0·207	0·207
F-2	4·677 (2)	5·588 (1)	5·004 (1)	0·202	0·197
G-1	4·664 (1)	5·577 (1)	4·997 (1)	0·195	0·179
C-4	4·723 (1)	5·597 (1)	5·021 (1)	0·227	0·223
A-1	4·721 (1)	5·596 (1)	5·023 (1)	0·223	0·217
E-4	4·710 (1)	5·592 (2)	5·019 (1)	0·215	0·205
B-3	4·705 (1)	5·586 (1)	5·015 (1)	0·208	0·194
B-4	4·716 (1)	5·590 (2)	5·021 (1)	0·219	0·207

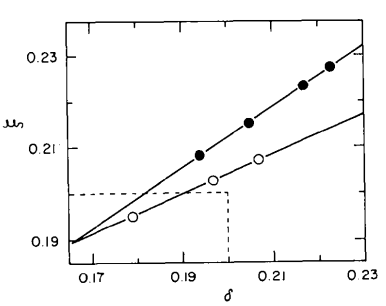

Fig. 3. Plots of ξ *versus* δ for the *I* phases. The filled circles correspond to the starting composition $Cr_2(Ti_{0.8}Zr_{0.2})_3O_9$ and the open circles to $(Cr_{0.8}Fe_{0.2})_2(Ti_{0.8}Zr_{0.2})_3O_9$. Progressive Cr loss by volatilization results in decreases in both ξ and δ.

time. This is partly due to the progressive loss of Cr from the samples by volatilization and is reflected in decreasing values for both ξ and δ. Graphs of ξ *versus* δ, Fig. 3, are linear over the relatively narrow ranges of values encountered, for samples with fixed Fe/Cr ratios. However, the slopes are different for *I* phases with [Fe]/([Fe] + [Cr]) = 0·00 and 0·20 respectively. A significantly anisotropic expansion of the subcell along $[100]_\alpha$ also accompanies the substitution of Fe for Cr in the *I* phases, *e.g.* compare *C*-2 and *C*-4 which were reacted under identical conditions; the observed changes in a_α, b_α and c_α are 0·96, 0·02 and 0·26% respectively. By comparison the anisotropy is much less marked within a series with fixed [Fe]/([Fe]

+ [Cr]) {Δa_α, Δb_α, Δc_α = 0·30, 0·34, 0·22 and 0·38, 0·20, 0·12% respectively between the end members of the series with [Fe]/([Fe] + [Cr]) = 0·00 and 0·20}.

I phases with simple fractional values of ξ and δ, *e.g.* $\xi = \delta = \frac{1}{3}$ (shown by the intercept of the dashed lines in Fig. 3), were not encountered in this work.

4. Idealized structural models for the *I* phases

Our approach in determining the structural principles underlying the series of *I* phases was to initially establish approximations to the structures with simple fractional values of ξ and δ, then to consider what modifications were necessary to explain the observed complex parameters.

Irrespective of the values for ξ and δ, certain features of the diffraction patterns were common to all the *I* phases and these were very useful in helping to establish structural models. First it was noted that reflections which lay on the nodes of the α-PbO_2 sublattice all corresponded to diffraction from oxygen planes of the α-PbO_2 structure, which are approximately hexagonal close-packed. These index as $(200)_\alpha$, $(040)_\alpha$, $(240)_\alpha$, in Fig. 2. By contrast the reflections which are predominantly due to the metal atoms in α-PbO_2, $(110)_\alpha$, $(020)_\alpha$, *etc.* ..., are all split into a number of components, separated from the sublattice nodes by distances which are linear combinations of the vectors ξ and δ; *i.e.* if we consider that the *I* phases have structures related to the α-PbO_2 type as the diffraction data suggest, then we can assume that the oxygen lattice remains essentially unchanged from that in α-PbO_2, but that there are periodic rearrangements in the metal atom arrangement. Secondly, the *c*-glide in α-PbO_2, space group *Pbcn*, and in ordered variants such as wolframite, space group *P*2/*c* (Keeling, 1957) and *M*-$LiTa_3O_8$, space group *C*2/*c* (Gatehouse, Negas & Roth, 1976), is retained in all the *I* phases.

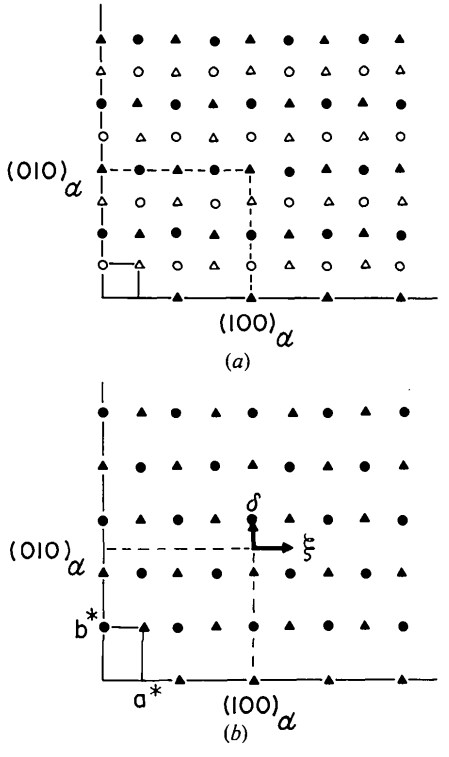

Fig. 4. Calculated reciprocal-lattice sections corresponding to (*a*) $\xi = \frac{1}{4}$, $\delta = \frac{1}{4}$ and (*b*) $\xi = \frac{1}{4}$, $\delta = \frac{1}{3}$. Open and closed triangles represent superlattice reflections ($h_\alpha \pm n.\xi$, $k_\alpha \pm m.\delta$, 0) associated with sublattice nodes with *h* and *k* odd, *h* and *k* even respectively. Open and closed circles represent superlattice reflections ($h_\alpha \pm n.\xi$, $k_\alpha \pm m.\delta$, 1) associated with sublattice nodes with *h* and *k* odd, *h* and *k* even respectively. In (*b*), the open and closed symbols superimpose.

Reciprocal lattices were constructed corresponding to various simple fractional values of ξ and δ, $1/n$, n = 4,5,6,7 which spanned the observed range of values; *i.e.* the patterns of superlattice spots radiating out from each of the α-PbO_2 sublattice nodes were reproduced, using the observed patterns as a guide, but using simple fractional submultiples of the sublattice spacings to define the superlattice spot positions. Typical examples are shown in Fig. 4. Note from these diagrams that when $\delta = 1/n$, n even, then δ corresponds to the separation between the superlattice rows and so the corresponding superperiod is simply $n \times b_\alpha$. However, for n odd, Fig. 4(*b*), δ equals half the separation between the rows of superlattice spots and the corresponding superperiod in real space is $(n/2) \times b_\alpha$.

The combination $\xi = 0{\cdot}25$, $\delta = 0{\cdot}20$, Fig. 4(*b*), gave particularly simple reciprocal-lattice geometry with an *I*-centred orthogonal cell, related to the α-PbO_2 subcell by $a = 4a_\alpha$, $b = \frac{5}{2}b_\alpha$, $c = c_\alpha$ and it was selected as a basis for a structural model. It soon became apparent that a sensible model based on the α-PbO_2 structure could not be constructed in orthorhombic space groups. Using the monoclinic space group *I*2/*c*, models were considered based on various ordered occupancies of the octahedral sites in a hexagonal close-packed anion framework. With the restrictions imposed by symmetry and by composition (*i.e.* stoichiometry close to $MO_{1{\cdot}80}$) a model was soon found that reproduced the observed intensity distribution for a typical *I* phase, Fig. 2(*a*) (but not of course the exact geometrical disposition of diffraction spots). A detailed refinement of this model was not considered worthwhile, as it corresponds to a ξ value, 0·25, which is considerably higher than any of the observed values. However, using this model as a guide, a model was quickly established corresponding to the more realistic but more complicated case where $\xi = \delta = 0{\cdot}20$, *i.e.* values within the observed experimental ranges. The model was established in the monoclinic space group *P*2/*c*, with $a = 5a_\alpha = 23{\cdot}53$, $b = \frac{5}{2}b_\alpha = 13{\cdot}97$, $c = c_\alpha = 5{\cdot}01$ Å, $\beta =$

90·00° and refined* using zero-level *hk*0 precession data for phase *E*-4, Fig. 2(*a*).

The derived structure is shown in projection down *c* in Fig. 5. It comprises blocks infinitely extended along $[010]_\alpha$ and $[001]_\alpha$ in which strings of corner-linked octahedra as in α-PbO_2, and face- and edge-shared octahedra as in Cr_2O_3 (corundum-type), alternate parallel to $[110]_\alpha$. The metal-atom arrangements in the blocks are mirrored across $(100)_\alpha$ planes at $x = 0$ and $x = \frac{1}{2}$ so that in adjacent blocks the α-PbO_2-like and corundum-like strings are alternatively parallel to $[110]_\alpha$ and $[1\bar{1}0]_\alpha$. Two types of 'metal mirror planes' occur. Those at $x = 0$ comprise α-PbO_2-like chains of edge-shared octahedra along $[001]_\alpha$ which are corner-linked to similar chains in the blocks on either side to produce 2 × 2 columns of α-PbO_2-type infinitely extended along $[001]_\alpha$. Four such blocks are shown centred at the corners of the unit cell outline in Fig. 5. Within the metal mirror planes at $x = \frac{1}{2}$, both α-PbO_2-like, $[001]_\alpha$ chains of edge-shared octahedra, and isolated octahedra occur. The latter corner-share with octahedra in six-membered edge-shared rings in the blocks on either side.

Within individual blocks, the alternation of α-PbO_2-like and corundum-like strings parallel to $\langle 110\rangle_\alpha$ in $(001)_\alpha$ planes is similar to that which occurs in the *E* phases. However, in the latter the strings are infinitely extended along $[110]_\alpha$. Furthermore, in successive $(001)_\alpha$ planes in the *E* phases, the octahedral strings are all oriented in the same direction whereas in the *I* phases, the strings are alternatively aligned along $[110]_\alpha$ and $[1\bar{1}0]_\alpha$ as a result of the *c* glide. For the structure shown in Fig. 5, the unit-cell composition is $M_{56}O_{100}$, *i.e.* $MO_{1.786}$, compared with a starting composition of $MO_{1.80}$, *i.e.* the formation of an *I* phase with $\xi = \delta = \frac{1}{5}$ requires partial reduction. This is consistent with the observation that the *I* phases are prepared more readily in nitrogen than in air.

The calculated F^2 for *hk*0 reflections based on the model shown in Fig. 5 are represented by the areas of the filled circles in Fig. 2(*b*). It is seen that the model closely reproduces the observed F^2 distribution, *cf.* the precession data (reduced to F^2's) for sample *E*-4, Fig. 2(*a*), but not of course, the exact geometrical disposition of diffraction spots, due to the approximations made that the values of ξ and δ were exactly $\frac{1}{5}$.

In the following section we will consider how the 'basis structure' shown in Fig. 5 must be modified to explain the observed ranges of ξ and δ in the *I* phases.

* Subsequently a full intensity data set for *B*-3 has been collected on a Philips PW1100 diffractometer and the structure has been refined to an *R* value of 0·075 for 1091 independent reflections. The refinement was complicated by partial disorder in some metal-atom sites and by fine-scale twinning (Grey, Marezio & Tranqui, to be published).

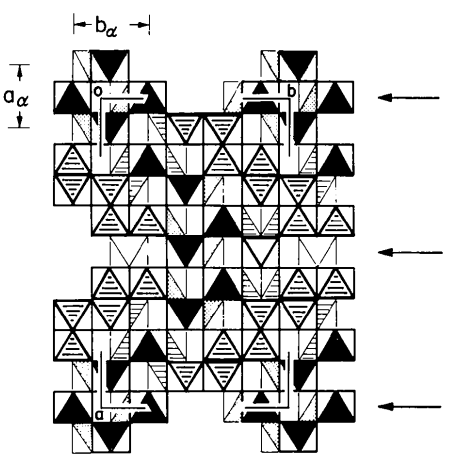

Fig. 5. The structure of an *I* phase in the approximation of $\xi = \delta = \frac{1}{5}$, viewed in projection along $[001]_\alpha$. The $\langle 110\rangle_\alpha$ corundum segments are shown with heavy horizontal hatching for metal atoms at $z = \frac{1}{4}$, light hatching for $z = \frac{3}{4}$; α-PbO_2 segments are shown, blocked, for $z = \frac{1}{4}$, stippled at $z = \frac{3}{4}$. Isolated octahedra in the layers at $x = 0$ and $\frac{1}{2}$ are shown unshaded. The unit cell is outlined. The metal mirror planes at $x = 0$ and $x = \frac{1}{2}$ are indicated by arrows.

5. Long-period intergrowth models

The results given in Table 4 and shown plotted in Fig. 3 suggest that the values of both ξ and δ vary continuously as a function of reaction conditions. The observed behaviour is similar to that described in the literature for modulated structures with incommensurate superperiods; *e.g.* in metallic conductors such as various alloys having long-period antiphase domain structures (Sato & Toth, 1961) and layered chalcogenides exhibiting charge density waves (Wilson, DiSalvo & Mahajan, 1975) the modulation wavelength is determined by the electronic structure of the material and is normally incommensurate with the sublattice period. It is often found to vary in a continuous manner with variation of parameters such as the electron/atom (*e*/*a*) ratio (Sato, 1979) and the temperature. Similarly, non-metallic compounds such as Na_2CO_3 (Brouns, Visser & de Wolff, 1965) and $Rb_2PbCu(NO_2)_6$ (Mori, Noda & Yamada, 1979) have modulated structures with wave vectors which are incommensurate with the periodicity of the original lattice and which vary continuously with temperature. In these cases, the continuously variable nature of the superlattice period is directly related to continuously varying structural parameters: the libration of CO_3 ions and Jahn–Teller distortions respectively.

In contrast, for the class of compounds studied here, the *I* phases, the observed superstructures result from different ordering patterns of octahedral site occupancies by metals, in an essentially close-packed oxygen lattice, *i.e.* the superstructures derive from different combinations of filled and empty sites and are thus

quantized rather than continuously variable. *Apparently* incommensurate superperiods can be explained in this case in terms of (incompletely) ordered long-period intergrowths between two or more basis structures which have periodicities which are simple multiples of a common subcell. This type of approach has been previously used to explain the observed one-dimensional 'incommensurate' superperiods in rutile-related intergrowth structures (Bursill, Grey & Lloyd, 1976) and in α-PbO_2-related intergrowths in the *E* phases (Grey *et al.*, 1973). Although the *I* phases display the added complexity of 'incommensurate' superperiods in two dimensions the same principles apply. Examination of electron-diffraction and X-ray diffraction patterns for the *I* phases failed to reveal the 'super-superlattice' reflections (Mann & Bevan, 1972) which would indicate perfect long-range intergrowth ordering, but the superlattice reflections were always sharp and well defined, and up to three orders were usually observed about the subcell nodes, indicating relatively high homogeneity of sample.

For the *I* phases, the basis structures for the long-period intergrowths are structures of the type shown in Fig. 5 for the particular case of $\xi = \delta = \frac{1}{5}$. Using this model as a guide, other basis structures are easily derived. Two examples are given in Figs. 6 and 7, for $\xi = \delta = \frac{1}{4}$, and $\xi = \frac{1}{6}$, $\delta = \frac{1}{7}$ respectively. Inspection of these diagrams shows that the change in ξ is effected simply by decreasing or increasing the lengths of the α-PbO_2-like and corundum-like strings of octahedra by one unit, *i.e.* the spacing between the metal mirror planes is decreased or increased by one $(100)_\alpha$ layer of octahedra.

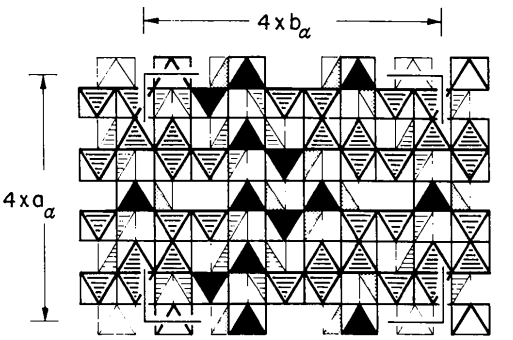

Fig. 6. The structure of an *I* phase in the approximation of $\xi = \delta = \frac{1}{4}$, viewed in projection along $[001]_\alpha$. Octahedra shading, *etc.*, as for Fig. 5.

Changes in δ result from introducing extra strings of either α-PbO_2-type or corundum-type, parallel to $\langle 110 \rangle_\alpha$. In Fig. 6 the introduction of a second corundum-like string of face- and edge-shared octahedra corresponds to $\delta = \frac{1}{4}$, *i.e.* to a superperiod of $4b_\alpha$. In Fig. 7 two α-PbO_2-like strings alternate with single corundum-like strings and $\delta = \frac{1}{7}$; the superperiod is $3{\cdot}5b_\alpha$. The values of ξ, δ corresponding to the models in Figs 6 and 7 are higher and lower respectively than any ξ, δ pair of values experimentally observed for the *I* phases and so in principle it is possible to derive models

Table 5. *I phases represented as long-period intergrowths – calculated parameters*

	C-2	*F*-2	*G*-1	*B*-4
Repeat along $[100]_\alpha$	$5 \times (5a_\alpha) + (4a_\alpha)^a$ $29a_\alpha$	$12 \times (5a_\alpha) + (4a_\alpha)$ $64a_\alpha$	$7 \times (5a_\alpha) + (6a_\alpha)$ $41a_\alpha$	$4 \times (5a_\alpha) + 3 \times (4a_\alpha)$ $32a_\alpha$
Repeat along $[010]_\alpha$	$10 \times (\frac{5}{2}b_\alpha) + (4b_\alpha)^b$ $29b_\alpha$	$25 \times (\frac{5}{2}b_\alpha) + (\frac{7}{2}b_\alpha)$ $66b_\alpha$	$7 \times (\frac{5}{2}b_\alpha) + 3 \times (\frac{7}{2}b_\alpha)$ $28b_\alpha$	$10 \times (\frac{5}{2}b_\alpha) + (4b_\alpha)$ $29b_\alpha$
$\xi_{calc.}$	0·2069	0·2031	0·1951	0·2188
$\xi_{obs.}$	0·207	0·2025	0·195	0·219
$\delta_{calc.}$	0·2069	0·1970	0·1786	0·2069
$\delta_{obs.}$	0·207	0·197	0·179	0·207
$O/M_{calc.}$	1·7837	1·7906	1·8036	1·7915
	C-4	*A*-1	*E*-4	*B*-3
Repeat along $[100]_\alpha$	$2 \times (5a_\alpha) + 3 \times (4a_\alpha)$ $22a_\alpha$	$5a_\alpha + 4a_\alpha$ $9a_\alpha$	$2 \times (5a_\alpha) + (4a_\alpha)$ $14a_\alpha$	$4 \times (5a_\alpha) + (4a_\alpha)$ $24a_\alpha$
Repeat along $[010]_\alpha$	$2 \times (\frac{5}{2}b_\alpha) + (4b_\alpha)$ $9b_\alpha$	$6 \times (\frac{5}{2}b_\alpha) + 2 \times (4b_\alpha)$ $23b_\alpha$	$14 \times (\frac{5}{2}b_\alpha) + (4b_\alpha)$ $39b_\alpha$	$13 \times (\frac{5}{2}b_\alpha) + (\frac{7}{2}b_\alpha)$ $36b_\alpha$
$\xi_{calc.}$	0·2273	0·2222	0·2143	0·2083
$\xi_{obs.}$	0·227	0·223	0·215	0·208
$\delta_{calc.}$	0·2222	0·2174	0·2051	0·1944
$\delta_{obs.}$	0·223	0·217	0·205	0·194
$O/M_{calc.}$	1·7838	1·7845	1·7902	1·7963

(*a*) Basis structures with repeats along $[100]_\alpha$ of $4a_\alpha$, $5a_\alpha$ and $6a_\alpha$ are shown in Figs. 6, 5 and 7 respectively. (*b*) Basis structures with repeats along $[010]_\alpha$ of $4b_\alpha$, $\frac{5}{2}b_\alpha$ and $\frac{7}{2}b_\alpha$ are shown in Figs. 6, 5 and 7 respectively.

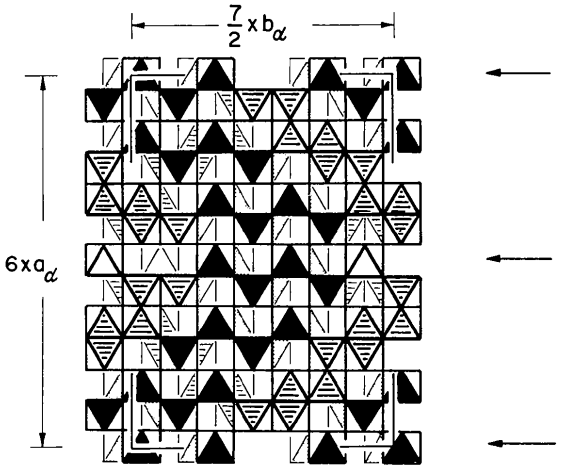

Fig. 7. The structure of an *I* phase in the approximation of $\xi = \frac{1}{6}$, $\delta = \frac{1}{7}$, viewed in projection along $[001]_\alpha$. Octahedra shading, *etc.*, as for Fig. 5.

corresponding to each of the observed ξ, δ combinations in Table 4 by suitable intergrowths of the components of the basis structures shown in Figs. 6 and 7 with the components of the intermediate basis structure shown in Fig. 5.

Table 5 gives a list of possible long-period intergrowths corresponding to the *I* phases listed in Table 4. The components of the basis structures forming the intergrowths are represented by their periodicities along $[100]_\alpha$ and $[010]_\alpha$, *i.e.* $4a_\alpha$, $5a_\alpha$ and $6a_\alpha$ corresponding to $\xi = 0{\cdot}25$, $0{\cdot}20$ and $0{\cdot}167$ and $4b_\alpha$, $\frac{5}{2}b_\alpha$ and $\frac{7}{2}b_\alpha$ corresponding to $\delta = 0{\cdot}25$, $0{\cdot}20$ and $0{\cdot}143$ respectively. The calculated values of ξ and δ* all agree with the experimental values to better than 0·001, which is the error in the measured numbers.

Most of the intergrowths are simple combinations of the basis-structure elements, such as 1:1, 2:1, 2:3 and 4:1, although some of the sequences have very long periodicities, *e.g.* 25:1 giving $b = 66b_\alpha \simeq 370$ Å, for sample *F*-2. When the superperiod for the intergrowth sequence is long the probability of maintaining the order over one unit cell is very small. Mistakes will invariably occur in the sequences and truly incommensurate spacings will occur if the mistakes are random (*i.e.* the long-period intergrowth required to allow the assignment of integral indices becomes infinitely long).

On the basis of a long-period intergrowth model for the *I* phases an estimate can be made of their stoichiometries (O/*M* ratios) from the stoichiometries of the contributing basis structures, *e.g.* for the basis structures shown in Figs. 5–7 the unit-cell compositions are $M_{56}O_{100}$, $M_{72}O_{128}$ and $M_{92}O_{168}$, with corresponding O/*M* ratios of 1·786, 1·778 and 1·826. The calculated O/*M* ratios for the long-period intergrowth approximations to each of the *I* phases are given in Table 5. They are lower than the corresponding values given in Table 2, which are calculated from the analytical results. The difference may be explained by partial reduction ($Fe^{3+} \rightarrow Fe^{2+}$, $Ti^{4+} \rightarrow Ti^{3+}$) which was not allowed for in the analytical results of Table 2.

6. Structure–composition relations in the *I* phases

The results given in Table 5 show interesting correlations between the O/*M* ratio in the *I* phases and the parameters ξ and δ; increasing reduction of the samples is accompanied by increasing values of both ξ and δ. These trends may be explained in terms of the structural response to the simultaneous requirements of stoichiometry balance and Zr/Ti ordering in the α-PbO_2 segments of the intergrowth structures. The latter requirement may be better understood by first considering the effects of Zr/Ti substitution in the related *E* phases.

Zr-substitution in the E phases

The general formula for the *E* phases is $(Cr,Fe)_{2p}$-$(Ti,Zr)_{p+2q}O_{5p+4q}$. In the absence of Zr, *E* phases are stable in the composition range $MO_{1{\cdot}67}$ ($p = 1$, $q = 0$) to $MO_{1{\cdot}80}$ ($p = 1$, $q = 1$) (Grey *et al.*, 1973). Replacement of about 20 at.% of Ti by Zr stabilizes compositions to higher O/*M* ratios, *i.e.* in the range $MO_{1{\cdot}82}$ to $MO_{1{\cdot}88}$. However, *E* phases containing more than a few at.% Zr cannot be prepared with compositions at or below $MO_{1{\cdot}80}$. The structure corresponding to this critical composition, $(Cr,Fe)_2Ti_3O_9$, is an ordered 1:1 intergrowth of α-PbO_2-type and V_3O_5-type structures, parallel to $(110)_\alpha$, *i.e.* $(110)_\alpha$ planar slabs of the two structure types alternate on the finest possible scale. For compositions more oxidized than $MO_{1{\cdot}80}$, *i.e.* $p > q$, the increased O/*M* ratio is accommodated by increasing the width of the α-PbO_2 segments which are intergrown with single-width blocks of V_3O_5-type. These structures are stabilized by the partial replacement of Ti by Zr. On the other hand, for compositions more reduced than $MO_{1{\cdot}80}$ the decreased O/*M* ratio corresponds structurally to increased widths of V_3O_5 segments which are intergrown with single-octahedra-wide $(110)_\alpha$ layers of α-PbO_2 type. These phases will not accept more than a few percent substitution of Zr for Ti. Increased Zr content in these phases leads to their transformation to the *I* phases, where larger (*i.e.* two-octahedra wide) segments of

* In Table 5, ξ and δ are as defined in Fig. 2(*a*) and the intergrowth periodicities along $[100]_\alpha$ and $[010]_\alpha$ are $(n/\xi) \times a_\alpha$ and $(m/\delta) \times b_\alpha$ respectively, where n and m are the smallest integers required to render n/ξ and m/δ integral. Note that when both m and m/δ are odd numbers, the actual intergrowth periodicity along $[010]_\alpha$ is halved, *i.e.* equal to $(m/2\delta) \times b_\alpha$. A simple example is given in Fig. 4(*b*) where $m = 1$, $m/\delta = 5$ and the superperiod is $\frac{5}{2} \times b_\alpha$.

α-PbO_2-type structure are incorporated at the metal mirror planes as shown in Figs. 5–7.

These observations suggest that Zr orders into the α-PbO_2 part of the intergrowth structures, and that this is possible only when the $(110)_\alpha$ segments are at least two-octahedra wide (*i.e.* contain a complete α-PbO_2 subcell). It appears that the single-octahedra-wide $(110)_\alpha$ planes of α-PbO_2 type do not have the necessary flexibility to accommodate Ti/Zr ordering, even on a short-range basis.

Structure–composition relations in the I phases

The relationship between the structure changes and composition changes are apparent from Table 5. The increase in the O/*M* ratio brought about by the loss of Cr_2O_3 is accompanied by decreases in both ξ and δ. Structurally, this corresponds to an increase in the widths of the blocks of α-PbO_2-corundum intergrowths along $[100]_\alpha$ and also to an increase in the ratio of α-PbO_2-type to corundum-type elements within the blocks. The latter is easy to understand; it is analogous to the increase in the ratio of α-PbO_2- to V_3O_5-type elements in the structures of the *E* phases, as the O/*M* ratio is increased. However, the increase in the widths of the intergrowth blocks in response to the oxidation is contrary to what one would expect on purely stoichiometric grounds. The $(100)_\alpha$ 'metal mirror planes' have a considerably higher O/*M* ratio than the intervening blocks of α-PbO_2-corundum intergrowths, and so increasing the separation between these planes (decreasing ξ) leads to a *reduction* in the O/*M* ratio, *i.e.* just the opposite of what is observed in Table 5. In order to explain this apparently contradictory behaviour it is necessary to consider the influence of composition factors other than the O/*M* ratio on the ξ–δ relationship. Among these, the requirement of Zr ordering in the α-PbO_2 columns seems to be an important factor.

Consider the effect of changing the variables ξ and δ in the *I* phases, subject to the restriction of approximately fixed Zr concentration, as is the case for the *I* phases listed in Table 5. As a starting model consider that shown in Fig. 5, with values of both ξ, 0·20, and δ, 0·20, in the middle of the observed range. The α-PbO_2-corundum-intergrowth blocks contain single-width α-PbO_2 strings alternating with single-width segments of corundum type. As discussed in the previous section, the Zr appears not to be able to order into the one-octahedra-wide α-PbO_2 strings and instead is expected to order into the 2 × 2 columns of α-PbO_2 structure at the metal mirror plane, producing a column of ordered α-PbO_2 as in wolframite (Keeling, 1957). Indeed, an indication of Zr ordering in the metal mirror planes was obtained from the structure refinement of the *I* phase, *B*-3 (Grey, Marezio & Tranqui, to be published), but the problem of partial disorder prevented an unambiguous determination of cation ordering.

Consider now the effect of an increase in the O/*M* ratio. This may be accommodated by increasing the ratio of α-PbO_2 segments relative to corundum segments in the intergrowth blocks, *i.e.* by *decreasing* δ. This can be achieved by replacing the single-octahedra-wide $[110]_\alpha$ strings by two-octahedra-wide segments as shown in Fig. 7 ($\delta = 0{\cdot}143$). Ordering of Zr can now occur within the intergrowth blocks. This means that less Zr needs to be accommodated in the $(100)_\alpha$ metal mirror planes and so their density decreases, or ξ *decreases*, corresponding to an increased separation of these planes.

The effect of *decreased* O/*M* ratio in the starting model cannot be explained by an equivalent argument. In this case the change in stoichiometry is accommodated by increasing the ratio of corundum structure to α-PbO_2 structure in the intergrowth blocks, *i.e.* corresponding to an *increase* in δ. The α-PbO_2-like $[110]_\alpha$ strings remain one-octahedra wide as δ is increased from 0·20 to 0·25 and so, within this entire range, the Zr atoms must order into the α-PbO_2 columns at the metal mirror planes. A comparison of Figs. 5 and 6 shows that with increasing δ, the density of α-PbO_2 columns in these planes decreases. Thus to accommodate the same concentration of Zr, there must be a higher density of metal mirror planes, *i.e.* their separation must decrease, corresponding to an *increase* in ξ. Thus the observed interdependence between δ and ξ can be qualitatively explained by the ordering requirements of the Zr atoms as the O/*M* ratio is changed.

The different curves for ξ *versus* δ for compositions with different [Fe]/([Fe] + [Cr]) ratios is difficult to explain. It is possible that the linear curves for the two sets of data shown in Fig. 3 are fortuitous and that in reality a single curve should be used for all the data, with a discontinuity at $\delta = 0{\cdot}20$. For δ values $> 0{\cdot}20$, there are no longer 2 × 2 columns of α-PbO_2 within the α-PbO_2-corundum intergrowth blocks and it is feasible that a more rapid rate of increase of ξ with increasing δ is necessary above this point.

Another possible reason for the two curves is that for the Fe-containing phases some of the Fe is divalent, and this large cation orders into the metal mirror planes. From Fig. 3 we see that for fixed δ, the Fe-containing series have higher ξ values, corresponding to more closely spaced metal mirror planes, which would be necessary if both Fe^{2+} and Zr^{4+} ordered into these planes. The ordering of large divalent Fe cations into the octahedral sites in the $(100)_\alpha$ planes may also be the reason for the observed anisotropic expansion of the α-PbO_2 subcell on replacement of Cr by Fe, where the maximum expansion was observed along $[100]_\alpha$, *i.e.* perpendicular to these planes.

However, the arguments put forward above are

speculative only, and the real situation can only be verified from the results of more detailed structural analyses of the *I* phases, using neutron diffraction to help establish the cation ordering. Powder neutron diffraction experiments are currently in progress.

I would like to thank Professor M. A. Alario, Chemistry Department, University of Madrid, for obtaining the electron diffraction patterns shown in Fig. 1 and Dr L. A. Bursill, Physics Department, University of Melbourne, for obtaining preliminary electron diffraction patterns on one of the samples. The careful analytical work of Ms C. Li (wet-chemical analyses) and Mr P. Kelly (microprobe analyses) is much appreciated. Mrs S. Foster and CNRS personnel are kindly thanked for the preparation of the manuscript.

References

BROUNS, E., VISSER, J. W. & DE WOLFF, P. M. (1965). *Acta Cryst.* **17**, 614.
BURSILL, L. A., GREY, I. E. & LLOYD, D. J. (1976). *J. Solid State Chem.* **16**, 331–347.
COUGHANOUR, L. W., ROTH, R. S. & DE PROSSE, V. A. (1954). *J. Res. Natl Bur. Stand.* **52**, 37–41
FLÖRKE, O. W. & LEE, C. W. (1970). *J. Solid State Chem.* **1**, 445–453.
GATEHOUSE, B. M., NEGAS, T. & ROTH, R. S. (1976). *J. Solid State Chem.* **18**, 1–7.
GREY, I. E. & MUMME, W. G. (1972). *J. Solid State Chem.* **5**, 168–173.
GREY, I. E. & REID, A. F. (1972). *J. Solid State Chem.* **4**, 186–194.
GREY, I. E., REID, A. F. & ALLPRESS, J. G. (1973). *J. Solid State Chem.* **8**, 86–99.
HAMELIN, M. (1957). *Bull. Soc. Chim. Fr.* pp. 1421–1439.
KEELING, R. D. (1957). *Acta Cryst.* **10**, 209–213.
LEE, C. W. (1970). *Ber. Dtsch. Keram. Ges.* **47**, 169–175.
MCQUEEN, R. G., JAMIESON, J. C. & MARSH, S. P. (1967). *Science*, **155**, 1401.
MANN, A. W. & BEVAN, D. J. M. (1972). *J. Solid State Chem.* **5**, 410–418.
MORI, N., NODA, Y. & YAMADA, Y. (1979). *AIP Conf. Proc.* No. 53 (*Modulated Structures*, Kailua Kona, Hawaii), pp. 214–216.
ROBINSON, B. W. & NICKEL, E. H. (1979). *Am. Mineral.* **64**, 1322–1328.
ROBINSON, S. C., EVANS, H. T., SCHALLER, W. T. & FAHEY, J. J. (1957). *Am. Mineral.* **42**, 619–628.
SATO, H. (1979). *AIP Conf. Proc.* No. 53 (*Modulated Structures*, Kailua Kona, Hawaii), pp. 165–167.
SATO, H. & TOTH, R. S. (1961). *Phys. Rev.* **124**, 1833.
SOMIYA, S., HIRANO, S. & KAMIYA, S. (1978). *J. Solid State Chem.* **25**, 273–284.
WILSON, J. A., DISALVO, F. J. & MAHAJAN, S. (1975). *Adv. Phys.* **24**, 117.

Acta Cryst. (1981). B**37**, 803–806

The Structure of Jasmundite,* $Ca_{22}(SiO_4)_8O_4S_2$

BY L. S. DENT GLASSER AND C. K. LEE†

Department of Chemistry, University of Aberdeen, Meston Walk, Old Aberdeen AB9 2UE, Scotland

(*Received* 20 *September* 1980; *accepted* 3 *November* 1980)

Abstract

Crystal structure analysis of a new mineral, tentatively named jasmundite, shows that it contains a mixture of orthosilicate, oxide and sulphide ions. The crystals are tetragonal, $I\bar{4}m2$, $a = 10{\cdot}461\ (1)$, $c = 8{\cdot}813\ (1)$ Å, $d_o = 3{\cdot}03$, $d_c = 3{\cdot}23$ Mg m^{-3}; cell content $Ca_{22}(SiO_4)_8O_4S_2$; $R = 0{\cdot}07$ for 637 observed reflexions. Three of the four independent Ca^{2+} ions have irregular octahedral coordination, with four contacts to the orthosilicate groups and two to the O^{2-} or S^{2-} ions. The fourth Ca^{2+} is eight-coordinated by O atoms of the orthosilicate group. The compound is unusual; structures containing a mixture of silicate and S^{2-} ions are rare. It is related to the compound alinite, $Ca_{22}[(Si_{0{\cdot}75}Al_{0{\cdot}25})O_4]_8O_4Cl_2$, which has been reported as a constituent of specialized cement clinkers.

Introduction

A new mineral rich in Ca and Si from Ettringer Feld, a lava flow of the Bellerberg volcano near Mayen, Eifel, was described by Hentschel (1968). Semiquantitative analysis indicated that the $CaO:SiO_2$ ratio was approximately 2:1, and S expressed as SO_3 was about 4%. It was suggested that the new mineral might be some form of Ca_2SiO_4 containing SO_4 groups. Semi-

* Name submitted to the IMA Commission on New Minerals.

† Present address: Chemistry Department, University of Agriculture, Serdang, Selangor, Malaysia.

0567-7408/81/040803-04$01.00